IOP PUBLISHING PHYSICS IN MEDICINE AND BIOLOGY

Phys. Med. Biol. **58** (2013) 2325–2348 doi:10.1088/0031-9155/58/7/2325

Viscoelastic Characterization of Elliptical Mechanical Heterogeneities Using a Semi-Analytical Shear-Wave Scattering Model for Elastometry Measures

Emmanuel Montagnon[†], Anis Hadj-Henni[†], Cédric Schmitt[†], Guy Cloutier[†,¥,*]

[†]*Laboratory of Biorheology and Medical Ultrasonics, Université de Montréal Hospital Research Center (CRCHUM), Montréal, Québec H2L 2W5, Canada; and Institute of Biomedical Engineering, Université de Montréal, Montréal, Québec H3C 3J7, Canada*

[¥] *Department of Radiology, Radio-Oncology and Nuclear Medicine, Université de Montréal, Montréal, Québec H3T 1J4, Canada*

[*] *Corresponding author: Prof. Guy Cloutier, Director, Laboratory of Biorheology and Medical Ultrasonics (www.lbum-crchum.com), Université de Montréal Hospital Research Center (CRCHUM), 2099 Alexandre de Sève, room Y-1619, Montréal, Québec H2L 2W5, Canada*

Dr A. Hadj-Henni and Dr C. Schmitt are now with Rheolution Inc. (www.rheolution.com), 5795 Avenue de Gaspé, #211, Montréal, Québec H2S 2X3, Canada

Keywords: Ultrasound imaging; Dynamic elastography; Shear wave imaging; Modeling; Elastometry; Rheometry; Biomechanics; Breast cancer.

Abstract: This paper presents a semi-analytical model of shear wave scattering by a viscoelastic elliptical structure embedded in a viscoelastic medium, and its application in the context of dynamic elastography imaging. The commonly used assumption of mechanical homogeneity in the inversion process is removed introducing *a priori* geometrical information to model physical interactions of plane shear waves with the confined mechanical heterogeneity. Theoretical results are first validated using the finite element method for various mechanical configurations and incidence angles. Secondly, an inverse problem is formulated to assess viscoelastic parameters of both the elliptic inclusion and its surrounding medium, and applied *in vitro* to characterize mechanical properties of agar-gelatin phantoms. The robustness of the proposed inversion method is then assessed under various noise conditions, biased geometrical parameters, and compared to direct inversion, phase gradient and time-of-flight methods. The proposed elastometry method appears reliable in the context of estimating confined lesion viscoelastic parameters.

1. Introduction

Mechanical properties of biological tissues may vary during pathological diseases/processes such as cancer (Samani *et al.*, 2007), fibrosis (Andersen *et al.*, 2009), or with heating (Bharat *et al.*, 2005). A wide variety of techniques has been developed to map tissue elasticity for diagnosis, screening or in the context of surgery (Parker *et al.*, 2011). Within the last twenty years, the ultrasound modality has been widely used to investigate mechanical properties of biological tissues (Lerner *et al.*, 1990; Ophir *et al.*, 1991). Static elastography takes advantage of the Hooke's law in the linear domain to establish relative strain maps, called elastograms. *In-vivo* studies using static elastography demonstrated the relevance of the technique for breast (Wojcinski *et al.*, 2010; Schaefer *et al.*, 2011) and prostate cancer screening (Castaneda *et al.*, 2009), despite operator dependency limitations. Shear wave elastography imaging (SWEI) (Sugimoto *et al.*, 1990; Rudenko *et al.*, 1996; Sarvazyan *et al.*, 1998) is another technique allowing quantitative estimation of the shear modulus, by assessing velocity of propagating shear waves. The concept has also been applied to magnetic resonance imaging (Muthupillai *et al.*, 1995; Plewes *et al.*, 2000; Sinkus *et al.*, 2005) and magnetic resonance elastography (MRE) has received attention in the last decade (Mariappan *et al.*, 2010).

Most inversion methods used in dynamic SWEI, such as the direct inversion (DI) (Sandrin *et al.*, 2002; Nightingale *et al.*, 2003; Catheline *et al.*, 2004; Bercoff *et al.*, 2004), the phase gradient (PG) (Chen *et al.*, 2004), and the time-of-flight (TOF) (Tanter *et al.*, 2008) methods rely on global or local mechanical homogeneity, linearity and isotropy assumptions. The DI method estimates the shear modulus by solving the Helmholtz equation from displacement spatial and time derivatives (Catheline *et al.*, 2004). PG and TOF methods estimate the shear wave speed from the phase shift or the time-of-arrival between two distant points to quantitatively assess the Young's elasticity modulus $E = 3\rho c^2$, where ρ is the density of the medium and c the estimated shear wave speed. The last two methods assume non-dispersive material because the shear wave tracking only allows assessing the group velocity (Tanter *et al.*, 2008; Palmeri *et al.*, 2008).

The major source of variability of the DI method is the computation of displacement numerical derivatives on noisy data to solve the Helmholtz's equation. Data filtering may thus be required to obtain reliable assessment (Nightingale *et al.*, 2003). For both PG and TOF methods, since the shear modulus is proportional to the square of the celerity, the variability follows the same quadratic non-linear relation, which increases for small regions of interest (Chen *et al.*, 2004). Moreover, during the propagation of shear waves, scattering and attenuation affect the wavefront pattern challenging tracking algorithms (McLaughlin *et al.*, 2006). To minimize those effects, directional filtering has been proposed (Deffieux *et al.*, 2011), allowing suppression of reflected waves in tracked patterns. Another alternative is to take into account the pattern of shear wave spreading along the propagation path (Klein *et al.*, 2012).

Since biological tissues are not purely elastic but viscoelastic, viscous effects have been introduced in theoretical models. Viscosity is related to the shear wave attenuation during propagation and to dispersion (*i.e*, the frequency dependence of the shear wave speed). For this goal, the DI method takes advantage of the imaginary part of the wavenumber (Catheline *et al.*, 2004), related to dissipative effects, whereas PG and TOF methods use dispersion curves (Chen *et al.*, 2004; Deffieux *et al.*, 2009). Another way to highlight viscous effects is to take advantage of the phase shift between applied stress and measured strain (Sridhar *et al.*, 2007; Vappou *et al.*, 2009).

In the breast cancer screening context, the distinction between benign and malignant lesions is challenging and often leads to unnecessary biopsies (Seltzer, 1997; Mitka, 2007). Such procedure induces stress for the patient (Jatoi *et al.*, 2006; Keyzer-Dekker *et al.*, 2012), and avoidable high costs to health systems (Greif, 2010). In this context, increasing diagnostic specificity using elastography is a recognized challenge with potential high impact (Berg *et al.*, 2012; Cho *et al.*, 2012). In the current work, it was assumed that low grade tumors can be described geometrically by ellipses (Madjar and Mendelson, 2008), and mechanically as viscoelastic materials. Such geometrical fitting of the shape of breast tumors has recently been proposed in static elastography, in the context of axial-shear strain imaging (Thittai *et al.*, 2010).

Therefore, the problem of shear wave scattering by viscoelastic elliptical inclusions was addressed and presented as a generalization of the circular case (Hadj Henni *et al.*, 2008). The manuscript is organized as follows: first, a semi-analytical model of shear wave scattering is presented and validated using the finite element method (FEM) for an inclusion softer or harder than the surrounding material. Then, an iterative inverse problem is formulated and applied to *in* *vitro* results obtained using agar-gelatin phantoms to provide elastometry mechanical measures. The robustness of the inversion method is finally presented considering input data with low signal-to-noise ratios (SNR) and biased geometrical parameters. The impact of the phase of the stationary displacement field on elastometry estimates was also evaluated. The viscoelastic characterization was done without any assumption on the rheological behavior of each material, and did not necessitate computation of numerical derivatives, likely improving robustness.

2. Methods:

2.1 Theoretical model:

Two dimensional (2-D) scattering of elastic plane shear waves by a viscoelastic elliptical structure (inclusion) embedded in an infinite viscoelastic surrounding medium is considered here (figure 1). The polarization vector is contained in the (*xy*)-plane (*i.e,* shear vertical waves or SV-waves). The incidence angle θ is defined as the angle between the incident wave vector and the *x*-axis, the latter corresponding to the large axis of the ellipse. In the following, subscript $j = \{incl, surr\}$ refers to the elliptic inclusion and surrounding medium, respectively. Time-dependence terms in $e^{i\omega t}$ are omitted and assumed understood. The complex shear modulus G_j can then be written as:

$$G_j = G_j^{'} + iG_j^{''} \qquad (1)$$

where $G_j^{'}, G_j^{''}$ are storage and loss moduli, respectively of medium *j*. Inserting (1) in the motion equation gives (Achenbach, 1973):

$$\rho_j \omega^2 \mathbf{U}_j + (\lambda_j + 2G_j)\boldsymbol{\nabla}(\boldsymbol{\nabla}.\mathbf{U}_j) - G_j \boldsymbol{\nabla} \times (\boldsymbol{\nabla} \times \mathbf{U}_j) = \mathbf{0} \qquad (2)$$

with ρ_j, ω, $\mathbf{U}_j$ and λ_j being respectively the density of medium *j* fixed at 1100 kg/m^3 for both media, the angular frequency, the displacement field, and the first Lamé coefficient. Using the Helmholtz decomposition and by considering φ as an irrotational scalar potential related to the compression wave, and $\boldsymbol{\psi}$ a vector potential describing the shear wave, one obtains:

$$\mathbf{U} = (U_x(x,y) \quad U_y(x,y) \quad 0)^T \ = \nabla\varphi + \nabla\times\boldsymbol{\psi} \tag{3}$$

Two Helmholtz equations are obtained by inserting (3) in (2) for both shear and compressional components of the displacement field (referred below by subscripts *S* and *C*, respectively). Namely,

$$\nabla^2\varphi_j + k_{Cj}^2\varphi_j = 0 \tag{4}$$

$$\nabla^2\boldsymbol{\psi}_j + k_{Sj}^2\boldsymbol{\psi}_j = 0 \tag{5}$$

In (4) and (5), longitudinal and transverse wavenumbers are respectively:

$$k_{Cj}^2 = \frac{\rho_j\omega^2}{\left(\lambda_j + 2G_j\right)} = \frac{\omega^2}{c_C^2} \tag{6}$$

$$k_{Sj}^2 = \frac{\rho_j\omega^2}{G_j} = \frac{\omega^2}{c_S^2} \tag{7}$$

with c_C and c_S the longitudinal and shear wave speeds, respectively.

According to the geometry considered, Helmholtz equations are solved in elliptical coordinates (Abramovitz and Stegun, 1965), where (η, ξ) are the angular and radial components, respectively. Using the separation of variable method, solutions of the Helmholtz equations in elliptical coordinates are expressed in terms of infinite series of angular and radial Mathieu functions (Chaos-Cador, 2002). A plane incident shear wave propagating in the infinite surrounding medium with an incidence angle θ is thus expressed in elliptical coordinates as:

$$\Psi_{inc} = \sum_{p} \sum_{n=0}^{\infty} 2i^{n} ce_{n}^{p}(\eta, q_{surr,S}) Ce_{n}^{p}(\xi, q_{surr,S}) ce_{n}^{p}(\theta, q_{surr,S}) \qquad (8)$$

$$\varphi_{inc} = 0$$

where $ce_n^p(\eta, q_2)$, $Ce_n^p(\xi, q_2)$ are respectively angular and radial Mathieu functions of order *n*, with parity $p = 0,1$ for even and odd functions, respectively. In (8), $q_{surr,S}$ is a dimensionless parameter that depends on the geometry and mechanical properties of the medium through the wavenumber (Chaos-Cador, 2002). It is given by:

$$q_{surr,S} = \frac{f^{2} k_{S,surr}^{2}}{4} \qquad (9)$$

where $f = \sqrt{a^2 - b^2}$ with *f*, the distance interfoci of the considered ellipse, and *a, b* its large and small half axes, respectively. Refracted waves, which are regular at the origin, are described using radial Mathieu functions of the first kind, whereas scattered waves, which are outgoing waves are expressed in terms of radial Mathieu functions of the third kind, called Mathieu-Hankel functions. Scalar and vector potentials of both refracted and scattered waves can therefore be expressed as:

$$\Upsilon_{j}^{kr} = \sum_{p} \sum_{n=n_0}^{\infty} A_{npk}^{j}(\omega) ce_{n}^{p}(\eta, q_{jk}) Ce_{n}^{rp}(\xi, q_{jk}) \qquad (10)$$

where $k = \{C, S\}$ refers to longitudinal and transverse wave polarization, respectively, $r = \{1,3\}$ denotes the kind of radial Mathieu function used. The parameters q_{jk} are determined from (9) using wavevectors expressed in (6)-(7). In (10), $n_0 = \{0,1\}$ is the first order of computation for even and odd Mathieu functions, respectively, and A_{npk}^{j} are unknown scattering coefficients to be computed.

Since angular Mathieu functions of different *q* parameters are not orthogonal (due to existing mechanically different media, as in the present case), the angular dependency cannot be easily removed as in the circular case (Faran and James, 1951; White, 1958). In this sense, it has been proposed to express angular Mathieu functions in the Fourier domain (Seyyed and Sanaei, 2008). Here, the difficulty is overcome by writing elastic boundary conditions, *i.e.* the continuity of both radial and tangential components of displacement and stress, over a finite set of points along the elliptic contour $\xi = \xi_0$:

$$\begin{aligned} U_{\xi_{incl}}\Big|_{\xi=\xi_0} - U_{\xi_{surr}}\Big|_{\xi=\xi_0} &= 0 \\ U_{\eta_{incl}}\Big|_{\xi=\xi_0} - U_{\eta_{surr}}\Big|_{\xi=\xi_0} &= 0 \\ \sigma_{\xi\xi_{incl}}\Big|_{\xi=\xi_0} - \sigma_{\xi\xi_{surr}}\Big|_{\xi=\xi_0} &= 0 \\ \sigma_{\xi\eta_{incl}}\Big|_{\xi=\xi_0} - \sigma_{\xi\eta_{surr}}\Big|_{\xi=\xi_0} &= 0 \end{aligned} \qquad (11)$$

Assuming a homogeneous isotropic and linear medium, second order stress and strain tensors are expressed respectively as:

$$\bar{\bar{\boldsymbol{\sigma}}} = \lambda(\nabla.\mathbf{U})\mathbf{I} + 2G\bar{\bar{\boldsymbol{\varepsilon}}} \qquad (12)$$

$$\bar{\bar{\boldsymbol{\varepsilon}}} = \frac{1}{2}(\nabla\mathbf{U} + \mathbf{U}\nabla) \qquad (13)$$

where **I** is the identity matrix. Inserting (10) in (12) and (13) allows writing (11) as a linear system of equations under the form **A x = b**, **x** containing unknown scattering coefficients introduced in (10). Each line of **A** describes one boundary condition of (11) expressed at one discrete point of the elliptic contour ($\xi = \xi_0, \eta \in [0, 2\pi]$). Since the displacement field in the surrounding medium is the sum of the incident and scattered displacement fields, known incident terms are indexed in **b** for each boundary condition. Finally, solving the formulated system allows thereafter the computation of both refracted and scattered waves at any point in space using (3) and (10). Details on the construction of the linear system are provided in Appendix.

2.2 Simulations with the finite element method:

The geometry of figure 1 and mechanical configurations listed in table 1 were implemented using the finite element method (COMSOL Inc., Burlington, MA, USA, ver. 3.3) in two dimensions, as considered in the theoretical model. The surrounding medium was modeled as a square region (20×20 cm^2). Plane shear wave generation was ensured by imposing a harmonic displacement at each node of the left boundary. To encounter the infinite medium assumption made in the theoretical model, *i.e.* to avoid undesired reflections on domain boundaries, mechanical absorbers were mimicked on the remaining three boundaries by imposing the same shear modulus as for the surrounding medium, but with an exponentially increasing viscosity with thickness. The thickness of mechanical absorbers was arbitrary defined as four wavelengths to allow vanishing of shear waves. The mesh element sizes were fixed at one quarter of a wavelength. The elliptical inclusion embedded in the surrounding medium was defined by specifying elastic boundary conditions (*i.e.*, stress and displacement continuity at the boundary). Both media were mechanically described as linear, homogeneous and isotropic.

2.3 Experiment protocol:

In vitro experiments were realized with two distinct one-liter agar-gelatin phantoms (product numbers G-1890 and A-9799 for gelatine and agar, respectively, Sigma Chemical, Saint-Louis, MO, USA), with mixture proportions given in table 2. The mechanical heterogeneity (inclusion) was a cylinder having an elliptic cross-section with major and minor radii of 5 mm and 3.8 mm, respectively. The ultrasonic beam-axis was oriented normal to the cylinder axis to assess displacements occurring in its cross-section (*xy*-plane). As presented in figure 2, transient excitation signals (typically 300 Hz central frequency, six-period long, weighted by a Hamming window) were generated by a function generator (model 33250A, Agilent, Palo Alto, CA, USA), then amplified (type 2706, low frequency amplifier, Brüel&Kjær) before supplying a vibrator (type 4810, Brüel&Kjær, Nærum, Denmark) mechanically linked to a plaque embedded in the phantom. To avoid any effects along the z-axis and hence encounter 2-D assumption formulated in both theoretical model and FEM simulation, z-axis dimensions of both plaque (120×120 mm^2) and cylinder (110 mm) were fixed more than ten times the major diameter of the inclusion

(10 mm). Radiofrequency data (RF-lines) were acquired using an ultrasonic scanner (Sonix RP, Ultrasonix Medical Corporation, Burnaby, BC, Canada) and a 10 MHz central frequency probe (model L14-5/38, 38 mm width, 128 elements, Ultrasonix Medical Corporation). Synchronization of excitation-acquisition sequences derived from an ECG-gated method (Chérin *et al.*, 2006) were trigged by the scanner computer and allowed achieving a reconstructed frame rate of 3850 Hz. Such frame rate was obtained by receiving data from only two elements of the probe over a 8-cm depth, while the transmission sequence consisted in 32-element aperture beams, with a 4-cm depth of focus (F-number = 4). To cover the whole probe width, 64 acquisitions were successively repeated, shifting active elements from 1 to 128. One thousand frames were acquired for each acquisition, and final images were reconstructed from the 64 acquisition sequences.

Displacements were estimated from RF data using a dedicated parallel 1-D normalized cross-correlation algorithm implemented on a graphical processor unit (GPU) (NVIDIA CUDA, 2008; Montagnon *et al.*, 2012). By taking advantage of the low latency of the GPU cache memory, the whole computing task was divided into blocks, each one processing data from one element of the ultrasound probe. This allowed quasi real-time processing of RF data, achieving a processing frame rate greater than 150 frames/sec for an 80×38 mm^2 field of view. From temporal transient displacements, the complex amplitude of each pixel at the excitation frequency was computed using temporal Fast Fourier Transforms (FFT) leading to complex stationary displacement maps (Schmitt *et al.*, 2011). Three acquisitions were realized for each phantom by translating the probe along the cylinder-axis (z-axis) over a minimum distance of two millimeters between each recording to consider data from various cylinder cross-sections. This allowed assessing the reproducibility of the proposed inversion method.

2.4 Inverse problem:

Due to the mechanical impedance contrast between the inclusion and surrounding medium, the incident shear wave is simultaneously refracted inside the inclusion and scattered in the surrounding medium. Displacements occurring in the inclusion thus depend on mechanical properties of both media; therefore, considering both media as one global system is of interest. In sake of generality, no assumption was made neither about the surrounding medium viscoelasticity nor about rheological models; consequently, the inverse problem allowed assessing shear storage and loss moduli of both media.

Initial viscoelastic moduli for both media were arbitrarily fixed to: $G_j = 10 + 0.1\, i\omega$ kPa, for $j = 1, 2$. This configuration describes a mechanically homogeneous medium and thus no *a priori* information about the elasticity contrast was introduced in the inversion process. Since experimentally assessed displacements are a projection of the real displacement vector on the ultrasonic beam axis, theoretical displacement components $\left(U_x, U_y\right)$ were projected on an axis corresponding to the experimental ultrasonic beam. Therefore, both displacement components assessed by the theoretical model were fully taken into account in the inversion process. Viscoelastic parameters of both media were finally estimated by minimizing a cost function using a non-linear least square solver. The cost function was formulated as the distance between normalized experimental and theoretical displacement profiles:

$$\left(G_{incl}, G_{surr}\right) = \arg\min\left\{ \left| \mathrm{Re}\left[\mathrm{U}^{T}\right] - \mathrm{Re}\left[\mathrm{U}^{E}\right] \right|^{2} \right\} \tag{14}$$

where Re indicates the real part operator, and $\mathrm{U}^{T}, \mathrm{U}^{E}$ are theoretical and experimental displacement profiles, respectively.

The minimum of the cost function (14) was determined using the non linear Levenberg-Marquardt least-square solver (*lsqnonlin* function of Matlab, The MathWorks Inc., Natick, MA, USA, version 6.5). The elliptical inclusion location was determined from B-mode images, allowing the definition of the elliptical system of coordinates, which origin coincided with the ellipse center. From Fourier transforms computed in Section 2.3, stationary experimental displacement profiles at 250 Hz and 300 Hz for "soft" and "hard" cases, respectively, were then extracted along the line normal to the ultrasonic beam axis (*i.e.*, along the image width) crossing the inclusion through its center (see figure 2). The phase was arbitrarily chosen to zero for the first point of considered displacement profiles (*i.e.*, at x = -2 cm). The effect of the phase on the inversion is discussed later in sections on robustness.

2.5 Robustness study

The robustness of the inversion method was first addressed by considering variability of estimated viscoelastic parameters from noisy input data. Normalized displacement profiles obtained by using the 'hard' configuration B in the FEM model were used as reference (table 1). A zero-mean random noise following a standard uniform distribution was added to the reference displacement profile and weighted to produce different SNRs. The noiseless data had an infinite SNR that was reduced to values between 22 and 10 dB. The SNR was computed from:

$$SNR = 20\log_{10}\left(\frac{RMS_{signal}}{RMS_{noise}}\right) \qquad (15)$$

where $RMS_{signal}, RMS_{noise}$ indicate the root mean square of the reference signal and added noise, respectively. For each SNR, the inversion algorithm was applied ten times, with a different random noise generation (new seed), at each iteration. Since breast tumors are mostly expected to be harder than surrounding tissues, robustness results are only presented for the hard case inclusion.

As mentioned earlier, the inversion method requires *a priori* on ellipse dimension (large radius a = 5 mm and small radius b = 3.8 mm) and location to define the elliptic coordinate system. The effect of those parameters on the inversion accuracy was also addressed by considering biased inclusion dimensions and locations for both soft (A_{Th}) and hard (B_{Th}) configurations used in the forward problem (table 1). Biased input values were expressed in percentage of the initial geometry and location, and errors on estimated mechanical parameters were computed using:

$$Err(\%) = \frac{X_{estimated} - X_{reference}}{X_{reference}} \qquad (16)$$

where $X_{estimated}, X_{reference}$ indicate estimated and reference values of either G'_{incl} or G''_{incl}. Additionally, an evaluation was conducted to test the influence of the phase of considered stationary displacement profiles on G'_{incl} and G''_{incl}. The inversion process was tested for various phase values in the range $[0;\pi]$ for both hard and soft configurations.

Mechanical configurations presented in table 1 are within the range of viscoelastic properties of agar-gelatin phantoms (Hadj Henni *et al*., 2011), which are known to exhibit low G''/G' ratios, also designated as $\tan\delta$. For biological tissues such as the liver, kidney or breast, $\tan\delta$ has been measured in the range [0.3; 0.6] (Sinkus *et al*., 2005; Valtorta *et al*., 2005). To assess robustness of the proposed method for such biological materials, two additional mechanical configurations (C_{Th} and D_{Th}) derived from A_{Th} and B_{Th} were simulated by specifying the inclusion loss modulus to half the shear modulus (*i.e*., G''/G' = 0.5).

3. Results:

3.1- Forward problem:

To simulate experimental configurations where induced displacements are parallel to the illuminating beam (figure 2), theoretical displacement vector components were projected along the *y*-axis of figure 1. Normalized displacement profiles obtained using the FEM and the semi-analytical model, using configurations of table 1, are presented in figure 3 (soft inclusion) and figure 4 (hard inclusion). Normalized root mean square errors (NRMSE) between the reference and the simulated profiles are 0.8% and 0.7% for the soft and hard cases, respectively. Those values become 3.5% and 5% when considering 2-D fields of view of 4 x 4 cm^2 centered on the ellipse. In figure 3, displacements are greater in the soft inclusion due to the lower shear modulus than in the surrounding medium. Furthermore, at the interface inclusion/surrounding medium, refracted waves are dominantly reflected with attenuated transmission to the surrounding medium due to the mechanical contrast impedance. Therefore, multiple internal reflections contribute to the enhanced displacements within the inclusion. As observed in (Hadj-Henni *et al.*, 2010; 2012), reflected waves in the inclusion lead to constructive interferences at specific frequencies, leading to a mechanical resonance phenomenon. For the hard inclusion case in figure 4, opposite trends are observed; due to the mechanical contrast, incident waves are predominantly reflected by the inclusion toward the external mechanical vibrator.

3.2- Inverse problem:

The experimental stationary displacement maps in the long-axis of the inclusion were used to formulate the inverse problem. To assess reproducibility, three data sets corresponding to three positions of the probe along the cylinder axis were processed for each phantom. Means and standard deviations of estimated storage and loss moduli are presented in table 3. Angles between the long-axis of the elliptic inclusion and the incident wave vector were -15º and 45º for the soft phantom *A* and hard phantom *B*, respectively. Such angle values were arbitrarily chosen in sake of generality aiming *in-vivo* application of the proposed method. By considering the estimated viscoelastic parameters in table 3, theoretical displacement maps are compared to experiments in figure 5 for the soft inclusion and in figure 6 for the harder one. The NRMSE between experimental displacement maps and theoretical ones computed from estimated viscoelastic parameters are 9% and 10% for soft (A_{Exp}) and hard (B_{Exp}) phantoms, respectively. Since shear wave speed increases with shear modulus, wavefronts are disturbed within the inclusion and either decelerate for the soft case or accelerate for the harder one, as seen in both theoretical and experimental maps.

3.3- Robustness study:

Estimated mechanical parameters for different noise amplitudes are presented in figure 7. Estimated shear moduli are little affected by noise (differences of 1.94% for the hard inclusion and 1.3% for the surrounding medium in the case of the minimum SNR of 10 dB). However, loss moduli are more variable with errors on mean assessments, at a SNR of 10 dB, of 16.4% and 11.6%, for the inclusion and surrounding medium, respectively. An example of solution for a SNR of 10 dB is presented in figure 8. With that noise magnitude, mean estimated storage moduli from 10 measures are 16670 ± 516 *Pa* for the inclusion and 2961 ± 24 *Pa* for the surrounding medium, instead of the simulated values of 17000 *Pa* and 3000 *Pa* for the same components. Estimated loss moduli are 786 ± 769 *Pa* and 168 ± 18 *Pa* instead of 940 Pa and 190 Pa, respectively.

Errors on estimated viscoelastic parameters in the case of biased large and small elliptic radii for both hard and soft configurations with $G''/G' = 0.05$ and $G''/G' = 0.5$ are presented in figure 9. Biases applied to both large and small axes range from -15% to 15% of initial ellipse dimensions. As seen in figure 9, the largest impact of the large axis dimension variation was on the accuracy of the inclusion loss modulus G''. It was maximum for the hard case inclusion at both G''/G' values. Errors for $G''/G' = 0.5$ were globally lower than for the low viscous configuration, especially for the hard configuration.

Changing the location of the inclusion (*i.e.*, of the displacement profile line used in the inversion process) was done by shifting the origin of the elliptical coordinate system along (x) and (y) axes from -15% to 15% of initial ellipse dimensions (figure 10). Again, largest errors were noted for G'' of the hard inclusion, especially for the low G''/G' ratio. Shear modulus estimations were little affected by biased location of axes, especially for y-axis shifts.

Figure 11 presents the impact of various phases of the reference stationary displacement profile on storage and loss moduli. As noticed for other abovementioned robustness tests, G' presented few variations, whereas G'' were more variable. The initial phase had the largest impact on G'' of the hard inclusion. Loss modulus estimation errors could achieve 90% for the low viscous inclusion (figure 11-a), but did not exceed 16% for $G''/G' = 0.5$ (figure 11-b).

4. Discussion:

4.1 Forward problem based on simulated results:

An excellent agreement between semi-analytical and FEM results was obtained for various configurations of viscoelasticity contrasts, incidence angles and frequencies. The main advantage of the semi-analytic simulation is the ability to compute displacement fields at any points in space, once scattering coefficients are determined, with a better time efficiency than FEM. This property makes the proposed approach relevant in a clinical context.

4.2 Inverse problem validation with phantoms:

The formulated inverse problem converged and allowed to assess viscoelastic parameters of both media with good reproducibility for the two phantoms. It is important to note that unlike the DI method, no spatial derivatives are needed in the proposed inversion algorithm; therefore no additional post-processing such as filtering of estimated displacements were required.

The accuracy of the solution depends on the formulated cost function (14). Here, we considered displacement profiles determined by the mechanical property of the inclusion and surrounding medium, and by the inclusion geometry. However, a challenge was to obtain reliable solutions for inclusion sizes at a fraction of the wavelength. Indeed, as one can see in figure 4 for the inclusion domain (between the two dashed lines), roughly half a wavelength is observed within the hard inclusion at the vibration frequency of 300 Hz. Estimating the loss modulus for the soft inclusion was less critical because close to a complete wavelength could be available at a frequency of 250 Hz, as seen in figure 3. Therefore, an inverse problem formulation estimating only inclusion mechanical parameters might be problematic and encounter more than one solution (*i.e.*, local minima). In our formulation, since the displacement profile was extracted along a line crossing both media (inclusion and surrounding medium), both reflected and scattered waves were taken into account to estimate viscoelastic shear moduli of both structures. Reflected waves are thus considered valuable in the inversion method. Such approach is at the exact opposite of directional filtering techniques (Deffieux *et al.*, 2011) where reflected waves are suppressed to minimize decorrelation in the shear wave tracking. Furthermore, the low NRMSE obtained between experimental and theoretical displacement maps demonstrate the goodness of estimated viscoelastic parameters. Thus, from a 1-D experimental displacement profile, the proposed method allowed estimating viscoelastic parameters of both media and retrieving 2-D maps.

4.3 Robustness study:

As one can see in figure 8, the elasticity estimation remained robust and not significantly affected by noise. Such robustness to noise is mainly explained by the 2-D formulation of the scattering phenomenon. Indeed, two *x*-*y* components of theoretical displacements are used to retrieve the 1-D displacement on which the inverse problem was formulated. Another explanation for robustness is the absence of numerical derivatives to assess the viscoelasticity. However, as discussed above, the inclusion loss modulus estimation was more sensitive to noise than the storage modulus assessment.

Introducing biased inclusion dimensions in the inverse problem did not affect drastically the storage modulus estimation for both configurations, whatever tan δ (figure 9). Indeed, despite geometrical variations, shear wave scattering occurs roughly under similar conditions compared to the unbiased case. However, while errors on loss modulus for the soft A_{Th} case remained acceptable for geometrical variations within ±15%, the hard inclusion exhibited large errors (figure 9). This trend for the B_{Th} case was generally reduced for the larger G''/G' ratio (figure 9-c, d).

Figure 10 reported errors on viscoelastic parameters related to biased inclusion locations, corresponding to an elliptical coordinate system not centered on the inclusion geometry. As in previous cases, the real part of the complex shear modulus remained stable, unlike the imaginary part, especially in the case of the inclusion stiffer than the surrounding medium at the low G''/G' ratio. Estimation errors related to changes in the reference displacement profile phase, presented in figure 11, exhibited the same general trends as in figures 9 and 10, *i.e.* that the loss modulus estimation for the low viscous condition was sensitive to input parameter variations. These observations naturally raise the question as to whether viscous parameters are really achievable using the proposed model for low G''/G' ratios, and more generally, does small inclusion viscosity really affect shear wave scattering for such conditions?

To address this question, we present in figure 12-a the reference profile obtained for the hard case using FEM and the theoretical profile computed from estimated parameters considering an initial phase of zero and G''/G' = 0.05. As notice, an excellent agreement is obtained (NRMSE = 0.7%), despite a large error on the estimated inclusion loss modulus (81.4%). Therefore, it clearly appears that for the hard inclusion configuration, its loss modulus has a very weak influence on observed displacement profiles. This can be explained by the fact that for a viscoelastic medium with a low tan δ, the loss modulus mainly affects displacement magnitude over distance and time. In the hard case, since the wavelength became greater than the inclusion dimension (λ = 1.13 cm for the example of figure 12-a), the decrease in displacement magnitude had little impact. In the case of the soft inclusion, the wavelength within its boundary was much smaller (λ = 0.59 cm), thus reducing errors in G'' estimates. Overall, the performance of the proposed inversion approach was improved for the case of more viscous contrast (*i.e.*, high tan δ).

According to our observations, errors on the inclusion loss modulus are expected to decrease in the case of larger inclusions, higher shear wave excitation frequencies, and higher tan δ. As an example, changing the excitation frequency for the hard configuration from 300 Hz to 450 Hz, which is still a frequency achievable in practice with shear wave imaging, the error in the estimate of the inclusion loss modulus dropped to 21 % (figure 12-b), which is roughly four times smaller than at 300 Hz. At the opposite, for very low frequencies, if wavelengths are larger than the inclusion dimension, no scattering occurs, and thus errors on viscoelastic parameters are expected to increase. This robustness study allowed highlighting key parameters for reliable viscoelastic measurements using the proposed method. First, at a constant G''/G' ratio, the loss modulus estimation is affected by the "elastographic signature", *i.e.* displacement profiles containing few but enough oscillations in both media, highlighting elastic and viscous effects through changes in wavelength and attenuation. Secondly, it has been shown that for poorly viscous media, despite excellent fittings (figure 12-a), errors can still achieve unacceptable values. However, considering materials with G''/G' ratios in the same range as those measured on biological tissues, both storage and loss moduli can be suitably assessed.

4.4 Approximation of the elliptic model by the cylindrical case:

In continuity of the above discussion on robustness, in the case the inclusion would be close to circular, a 2-D shear wave scattering model by cylinders (Hadj Henni *et al.*, 2008) would be applicable. However, to prove the flexibility of the current model and to assess how the cylindrical scattering model would depart from expected results in the case of elliptical inclusions with different b / a ratios (*i.e.*, different ellipticities), displacement profiles of the current study were fitted to both models. The circular inclusion with radius r was matched to the area of the ellipse by using $r = \sqrt{ab}$. Results for the hard configuration B_{th} (table 1) and G''/G' = 0.05 or 0.5 with b / a ratios from 0.40 to 0.76 are plotted in figure 13. Errors reported using the circular model are highly variable and most results are irrelevant. Such errors can be explained by the combination of the inability of circular Bessel functions (see Hadj-Henni *et al*., 2008) to describe displacement fields related to elliptical geometries, and the presence of local minima during the inversion process. For the elliptical model, b / a ratios were obtained by decreasing small axis values. An increase in estimation errors is observed for low b / a values. This can be explained bacause for "flat" ellipses, the small axis dimension is smaller than the incident wavelength and thus scattering is barely inexistent. In such cases, increasing the excitation frequency, and thus reducing incident wavelengths, is expected to provide better accuracy. Nevertheless, this figure clearly highlights limitations of the cylindrical model and demonstrates the flexibility of the elliptical one to fit different tumor geometries.

4.5 Comparison with other dynamic elastography methods:

To assess the impact of the mechanical homogeneity and one dimensional displacement assumptions on the inversion accuracy in the case of a heterogeneous medium, the DI (Sandrin *et al*., 2002; Bercoff *et al.*, 2003; Nightingale *et al.*, 2003) and PG (Chen *et al.*, 2004) methods (both aiming quantitative estimation of the complex shear modulus) were implemented and applied to previously validated displacement profiles presented in figure 4. The goal was not to presume on the relevance or validity of those algorithms in other elastography contexts, but to highlight consequences of assuming mechanical homogeneity in the case of a heterogeneous medium, without directional filtering. We recall here that DI and PG methods have been applied to map elasticity even in the case of heterogeneous media through spatial variations of shear wave speeds (ignoring diffraction and scattering effects), while the present approach requires the inclusion geometry to be known and assumes its homogeneity within the heterogeneous medium in order to take into account physical interactions. As mentioned earlier, low noise and high frequency sampling are required to compute numerical derivatives. Here, noiseless analytical displacements are considered, with a spatial sampling of 0.2 mm (less than roughly the 0.3 mm pitch of the probe). From the Helmholtz equation, the shear wave celerity corresponding to the direct inversion method was assessed as (Nightingale *et al.*, 2003):

$$k(\omega) = \sqrt{\frac{-\Delta U(x,\omega)}{U(x,\omega)}} \tag{17}$$

$$c(\omega) = \frac{\omega}{\mathrm{Re}(k(\omega))} \tag{18}$$

The phase gradient inversion method was applied on the same datasets; the celerity of shear waves was computed as (Chen *et al.*, 2004):

$$c_s = \frac{\omega \Delta r}{\Delta \phi} \tag{19}$$

with ω the angular frequency and $\Delta\phi$ the phase shift between two points separated by a distance Δr, fixed to 1 mm in this case.

To provide fair comparisons, the time-of-flight (ToF) method with directional filtering was also implemented and applied to simulated data. As for phantom experiments, the temporal excitation signal was modeled as a 300 Hz transient plane shear wave with a length of six periods. The simulated frame rate was 4 kHz. Using the theoretical model, displacement profiles were computed over the frequency range of the excitation signal (as in Hadj Henni *et al*., 2008) and weighted by respective complex amplitudes in the Fourier domain. Transient temporal displacements resulting from shear wave interactions with the elliptic cylinder were retrieved through inverse Fourier transforms.

Directional filtering, as described in (Deffieux *et al*., 2011), was applied to simulated displacement profiles. Briefly, negative *k*-space components of the displacement spatio-temporal 2-D Fourier transform, which are related to reflected waves in the time domain, were set to zero. Directionally filtered temporal displacements were recovered by using inverse 2-D Fourier transforms. Shear wave pattern tracking was performed using a cross-correlation algorithm on filtered data. To increase the accuracy of the shear wave speed estimation, the cross-correlation function was oversampled ten times before maximum search. Finally, estimated shear moduli were obtained from estimated velocities using: $G` = \rho c^2$.

Results are presented in figure 14. As one can see, both DI and PG methods are affected by the presence of the mechanical heterogeneity. Particularly, the PG method presents strong oscillations over the whole profile. Those oscillations are most likely due to the presence of reflected and scattered waves. On the other hand, the DI method, despite the absence of noise and a high spatial resolution, highlights variability and underestimates the inclusion shear modulus by approximately 15%. In figure 14-b, the unwrapped phases of studied profiles are presented. Variations of the phase slope depending on the propagating medium were low, even with an elasticity contrast greater than 5. It is important to recall that an infinite medium is considered here; therefore all changes in wavefront are due to the inclusion only, which are unavoidable even in transient elastography. Therefore, DI and PG methods may appear more appropriate for large homogeneous areas because the inversion accuracy decreases in the presence of a mechanical heterogeneity since physical interactions are not taken into account. One has to note that results obtained using ten times oversampled data exhibited the same trends.

According to figure 14-c, the ToF method with directional filtering allowed good estimation of the inclusion storage modulus and inclusion delineation, but overestimated the surrounding storage modulus by about 40%. For this configuration, the ToF method clearly outperforms DI and PG. The incident wave was a plane shear wave propagating in a non dispersive medium, *i.e.* with equal group and phase velocities. Therefore, the shear wave pattern did not change when propagating in the surrounding medium. At the opposite, shear waves induced by an acoustic radiation force are affected by geometric scattering, thus leading to deformation of the induced shear wave pattern over the propagation path. Such behavior challenges pattern tracking methods (McLaughlin *et al*., 2006) and might affect elasticity maps. Furthermore, it has been demonstrated in (Tanter *et al*., 2008) that breast parenchyma highlighted frequency dependant shear wave speeds and thus can be considered as dispersive. As presented in (Deffieux *et al*., 2011), shear wave spectroscopy allows estimating shear wave speeds over a large frequency range. However, for dispersive confined mechanical heterogeneities such as tumors, errors on velocity measurements over short distances are expected to increase with frequency, likely affecting the accuracy of dispersion curve fitting.

4.6 Limitations and future perspectives

Since *in vivo* applications are ultimate goals, assuming a mechanically homogeneous surrounding medium along the whole probe width, as in our experiments, might be irrelevant and a source of noise in the inversion process. Considering multiple short displacement profiles or scattering patterns in the cost function might provide additional characteristic information about the inclusion. In the current form, the method is only applicable to visible lesions since an *a priori* on the geometry is needed. In the case of non-visible lesions, it would be feasible to use other elastography methods as an initial step, if one assumes that those methods provide a better detection than clinical B-scans (Hiltawsky *et al.*, 2001), for localization and geometrical fitting of the lesion. According to results previously obtained with various elastography methods, the ToF combined with directional filtering appears most suitable for inverse problem initialization in the case of non-visible lesions. The model of the current study can easily be extended to consider cylindrical waves either by using plane wave decomposition or by expressing incident shear waves as outgoing waves using Hankel functions (Stamnes, 1995). Such a model thus might be efficiently applied to radiation force experiments, especially in the case of supersonic shear imaging (SSI) excitations since plane waves are remotely induced (Bercoff *et al.*, 2004). Moreover, the proposed inversion strategy is not limited to ultrasound elastography and would be relevant to process magnetic resonance elastography data.

In term of computational time, the semi-analytical method proposed in this paper only requires solving one linear system (11), for computation of scattering coefficients and displacements at desired spatial positions (with 10). In the case of the FEM, the whole geometry must be considered (*i.e.*, surrounding medium, inclusion, boundary conditions). The FEM execution time depends on various parameters such as the mesh density, size of the surrounding medium and mechanical absorbers. Without claiming to provide a computationally optimized FEM model, one displacement profile computation, for the hard configuration, required 41.1 ± 0.85 seconds compared to 0.82 ± 0.11 seconds for the semi analytical model (mean and standard deviations obtained from 10 iterations). The computation time required for the inversion is related to various parameters, such as initial mechanical parameters or search ranges, and typically requires 90 seconds using the semi-analytical model, which barely equals two iterations of the finite element model.

The extension of this work to a three-dimensional scattering problem appears as a logical next step. However, such model would require the use of non-orthogonal spheroidal wave functions (Abramovitz and Stegun, 1965), discretization of three dimensional volumes, and finally inversion of large ill-conditioned systems. Moreover, on a practical point of view, estimating mechanical properties of 3-D structures would require a 3-D scan, then segmentation procedure and finally the assessment of the plane to display within the entire volume. Such procedure would considerably complicate the clinical exam. This question highlights the global trade off between estimation accuracy and algorithm complexity, with in mind clinical applications.

In this study, scattering coefficients were computed using discrete points along an elliptic contour. Malignant tumors are known to exhibit irregular contours (American College of Radiology, 2007). Because small fluctuations of the contour geometry are much smaller than considered wavelengths in elastography, this is not expected to induce major effects on shear wave scattering, and the elliptic contour approximation may still be valid (see Schmitt *et al*., 2013 for such assessment in the context of shear wave induced resonance elastography of deep vein thrombi). The model can consider more complex geometries by writing elastic boundary conditions on contours slightly different from an ellipse. However, in the case of very complex shapes, basic functions used to describe the displacement field might be irrelevant, leading to ill-conditioned linear systems. In those cases, FEM might be more appropriate.

5. Conclusion

In the context of viscoelastic characterization of confined mechanical heterogeneities, a semi-analytical model of shear wave scattering has been presented and validated. Experimental results demonstrated a good reproducibility and robustness to added noise. In our approach, the lesion geometry was an *a priori* measurable parameter that was fitted by ellipses and then used as an input parameter to the proposed model. Computing G' and G'' over a wide frequency range would allow the determination of the underlying general rheological model, which could be assessed *a posteriori*. At the opposite, viscoelasticity quantification methods using dispersion curves rely on *a priori* known rheological models (which choice may be unclear for biological tissues). To conclude, it is to note that the proposed plane incident wave model can be extended to consider cylindrical waves, offering perspectives for radiation force applications with *in situ* localized shear wave generation.

Acknowledgments

This research was jointly supported by the Natural Sciences and Engineering Research Council of Canada (grant #CHRP-365656-09) and the Canadian Institutes of Health Research (grant #CPG-95288).

Appendix

This appendix aims to detail the construction of the linear system used to describe the scattering of shear waves by ellipsoids. Let us first consider the first boundary condition expressed in (11), *i.e.* the continuity of radial displacements across the inclusion boundary. Both scattered and incident waves propagate through the surrounding medium. Therefore, one can write:

$$U_{surr} = U_{scattered} + U_{incident} \tag{20}$$

According to the Helmholtz decomposition (3):

$$U_{\xi} = \frac{1}{h}\left(\frac{\partial \varphi}{\partial \xi} + \frac{\partial \psi}{\partial \eta}\right) \tag{21}$$

with *h* a scale factor related to the coordinate system used:

$$\begin{aligned} h_{\xi} = h_{\eta} &= \boldsymbol{f}\left(\sinh^2 \xi + \sin^2 \eta\right)^{\frac{1}{2}} \\ h_z &= 1 \end{aligned} \tag{22}$$

From (11) rewrites as **A x = b**, (20) can be expressed in terms of infinite series of radial and angular derivatives of Mathieu functions. Due to the parity of Mathieu functions, each potential is described as a series of two distinct coefficients. Since displacements are a combination of two distinct potentials (see 3), four series of coefficients are to be computed for each component of displacements $\mathbf{U} = \left(U_{\xi}, U_{\eta}\right)$. Finally, eight series of unknown coefficients are determined and **x** is then a ($8N \times 1$) column-vector.

For each discrete point of the contour geometry defining the mechanical lesion, four boundary conditions were imposed to meet viscoelastic conditions defined by (11). Matrix **A** was built such that each row describes one boundary condition at one discrete point, leading to $4N_{pts}$ rows, with N_{pts} the number of discrete points considered in $8N$ columns. Owing to that, in order to obtain a square matrix, one can see that the number of contour points considered and the truncature order N are linked by a factor of 2. The matrix **A** of (11) thus has a dimension of ($2N \times 4N$).

As explained by Leon *et al.* (2004), the truncature order N depends on the "ellipticity" of the geometry and increases when ellipse flattens. N also depends on the product ka, with k the wavenumber and a the large axis of the ellipse. Considered frequencies and ellipse dimensions in our application typically lead to ka close to unit. We used $N = 25$, which is close to the value proposed by Leon *et al*. (2004): $N = 2N^* + 1$ with $N^* = ka + 10$.

Figures:

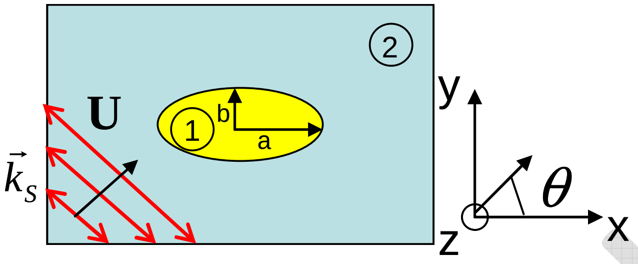

Figure 1 Geometrical configuration of the 2-D semi-analytical shear-wave scattering model. Plane shear vertical waves polarized along $\vec{k}_s$ (red arrows) propagate into an infinite medium 2, before impinging an elliptic inclusion 1, stiffer or softer than the surrounding medium. The dimensions of the inclusion are $a = 5$ mm and $b = 3.8$ mm.

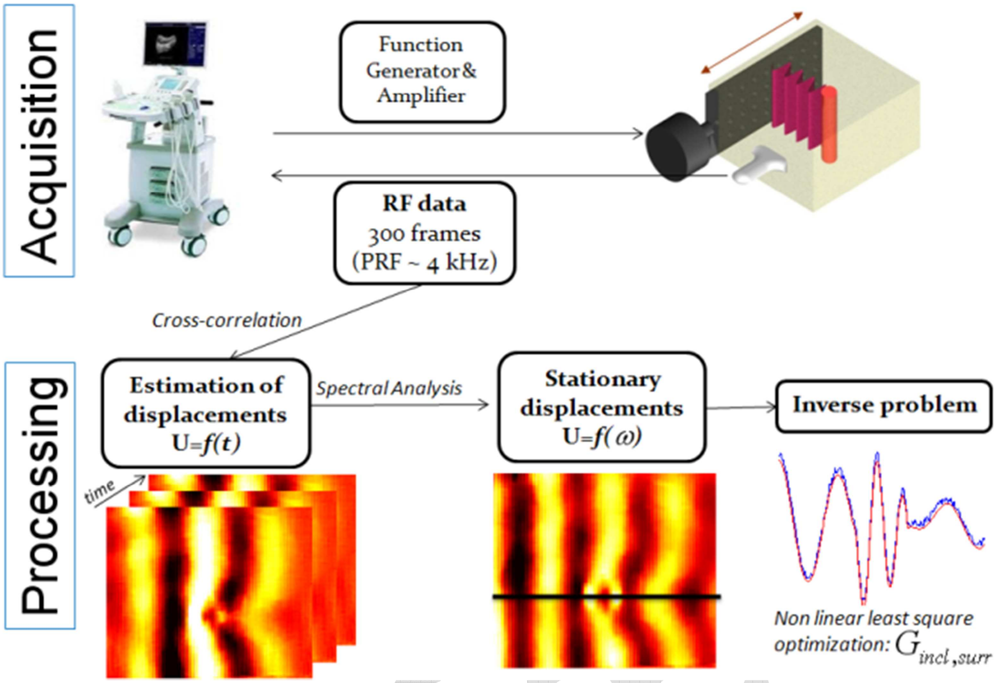

Figure 2 Flow chart of the experimental setup and data processing. Transient displacements are mechanically induced using a mechanical shaker. Those displacements are assessed from RF data acquired at an ultrafast frame rate using a standard 1-D cross-correlation algorithm. Stationary displacement maps are computed using Fourier transforms. Experimental displacement profiles are then extracted to compute the cost function defined as the distance between theoretical (U^T) and experimental (U^E) profiles.

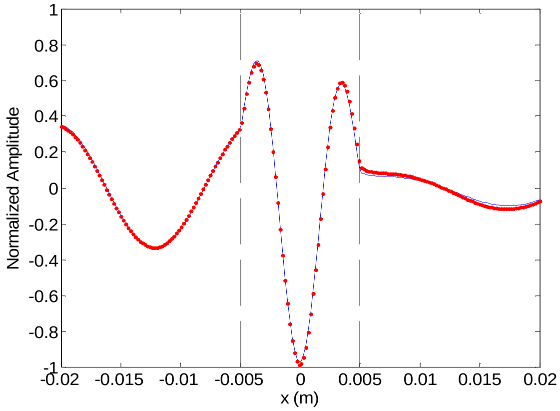

Figure 3 Normalized displacement profiles obtained by using the finite element method (dashed line) and the semi-analytical model (dots) in the case of a soft inclusion (configuration *A* of table 1). The NRMSE between both theoretical models was 0.8%.

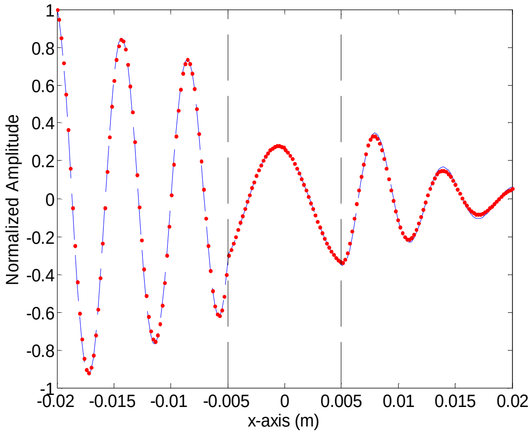

Figure 4 Normalized displacement profiles obtained by using the finite element method (dashed line) and the semi-analytical model (dots) in the case of a hard inclusion (configuration *B* of table 1). The NRMSE between both theoretical models was 0.7%.

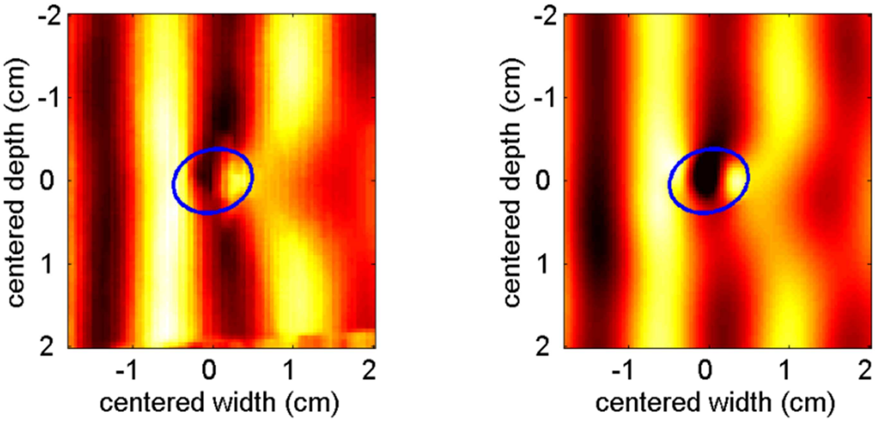

Figure 5 Experimental (left) and theoretical (right) stationary displacement maps obtained by using the solution of the inverse problem at 250 Hz (phantom *A* with a soft inclusion). The blue ellipse indicates the location of the inclusion insonified at an angle θ of -15 degrees. Field of view depth and width axes are centered on the ellipse.

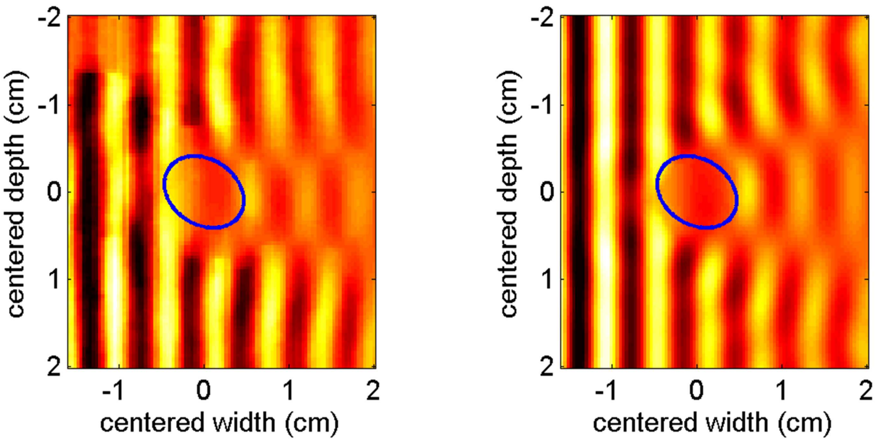

Figure 6 Experimental (left) and theoretical (right) stationary displacement maps obtained by using the solution of the inverse problem at 300 Hz (phantom *B* with a hard inclusion). The blue ellipse indicates the location of the inclusion insonified at an angle θ of 45 degrees. Field of view depth and width axes are centered on the ellipse.

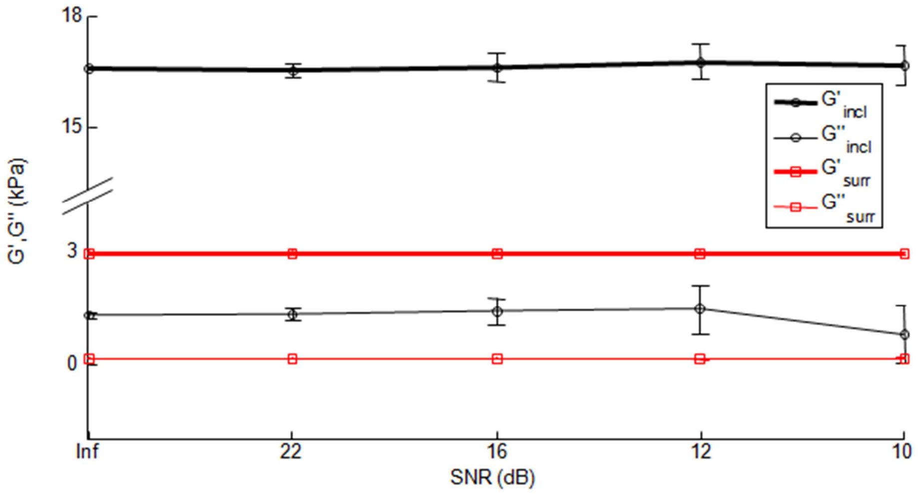

Figure 7 Viscoelastic parameters estimated for increasing noise amplitudes applied to FEM results in the case of the hard inclusion *B*. *G'* indicates the storage modulus, *G''* the loss modulus, the subscript *incl* refers to the inclusion, whereas the subscript *surr* indicates the surrounding material. The label *Inf* on the x-axis indicates an infinite SNR (*i.e.*, the zero noise condition).

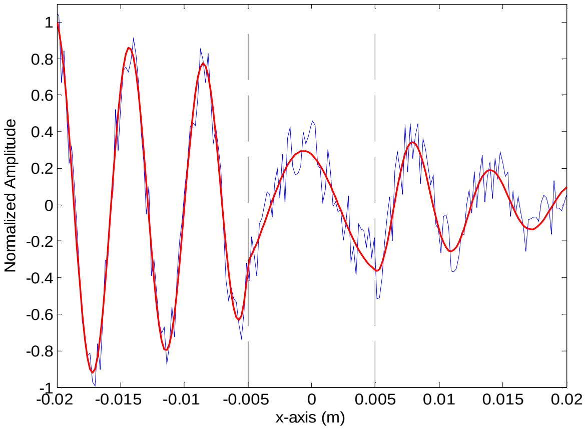

Figure 8 Theoretical displacement profiles obtained at the optimization convergence of the inverse problem for a signal-to-noise ratio (SNR) of 10 dB (red line) compared with simulated data corrupted with noise at the same SNR (blue line).

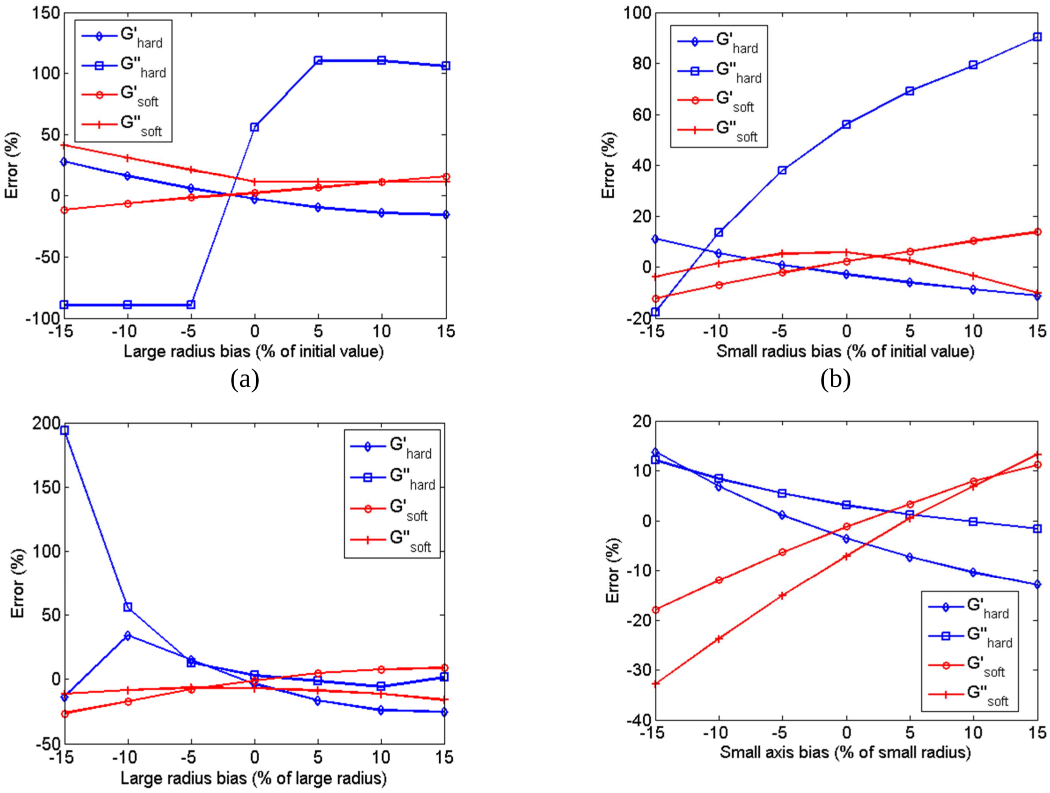

(a) (b)

(c) (d)

Figure 9 Errors on inclusion viscoelastic parameters (in % of reference values given in table 1) obtained by using biased ellipse large and small radii as inversion input parameters for soft and hard configurations with $G''/G' = 0.05$ (a, b) and $G''/G' = 0.5$ (c, d).

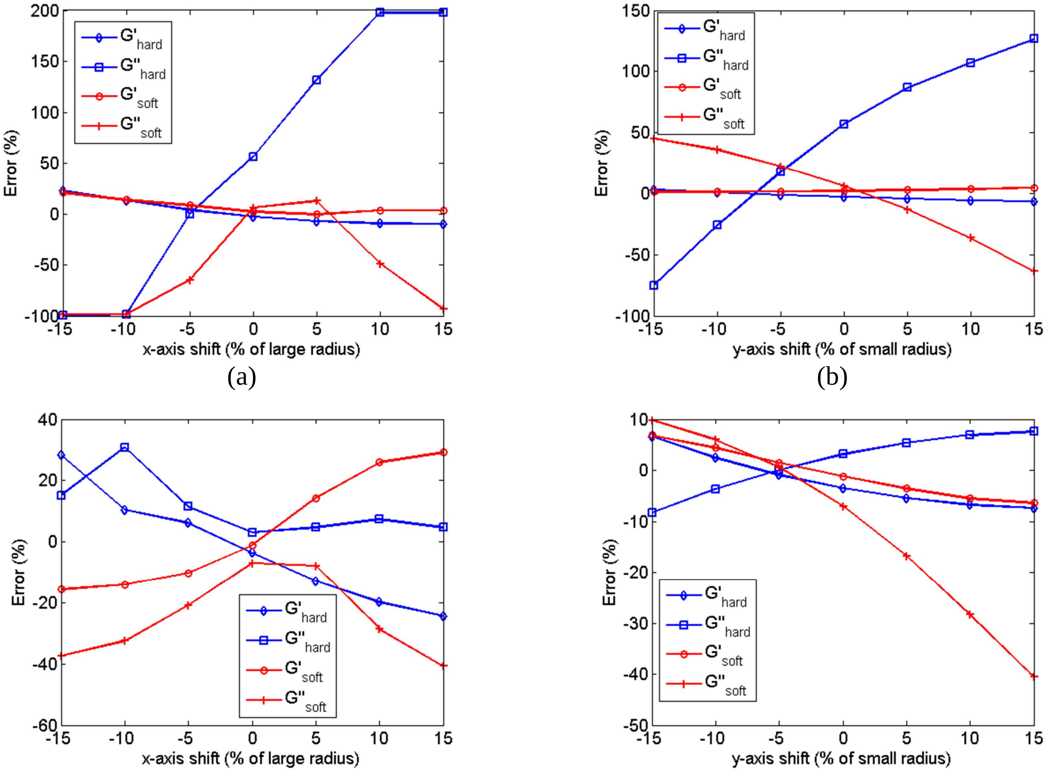

(a) (b)

(c) (d)

Figure 10 Errors on inclusion viscoelastic parameters (in % of reference values given in table 1) obtained by using biased inclusion locations along the *x*-axis and *y*-axis as inversion input parameters for soft and hard configurations with *G''*/*G'* = 0.05 (a, b) and *G''*/*G'* = 0.5 (c, d).

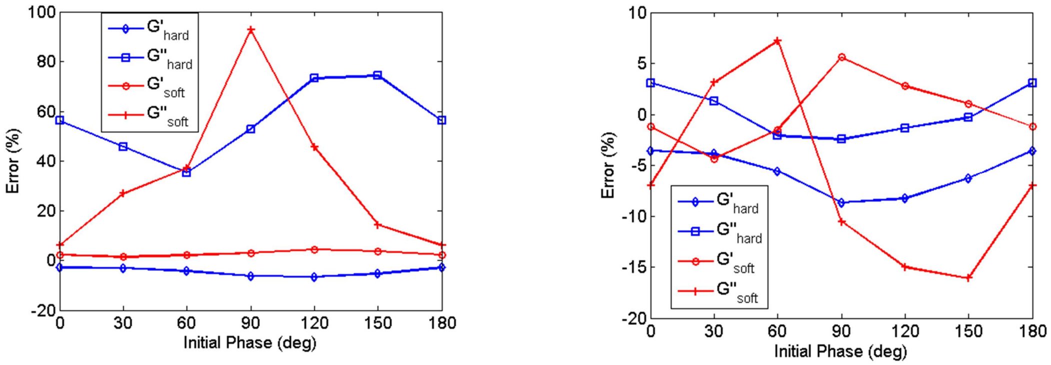

(a) (b)

Figure 11 Errors on inclusion viscoelastic parameters (in % of reference values given in table 1) obtained for various phases of the reference stationary displacement profile for soft and hard configurations with $G''/G' = 0.05$ (a) and $G''/G' = 0.5$ (b).

.

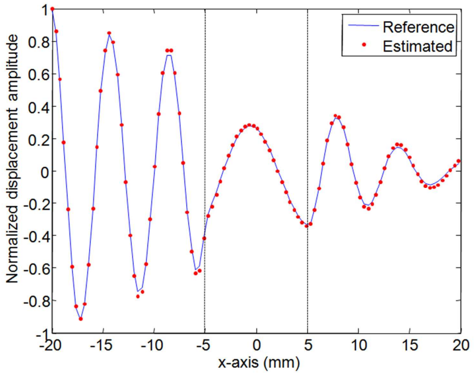

(a)

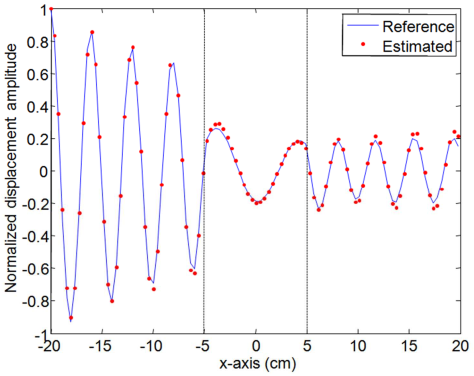

(b)

Figure 12 Reference (full line) and estimated (dots) displacement profiles at convergence of the optimization procedure for the hard inclusion case at 300 Hz (a); the NRMSE was 0.7% while the error on the inclusion loss modulus was 81.4%. Same as (a) but at 450 Hz (b); the NRMSE was 1.3% and the error on the inclusion loss modulus was 21.0%. The error on the inclusion loss modulus estimation decreases with frequency.

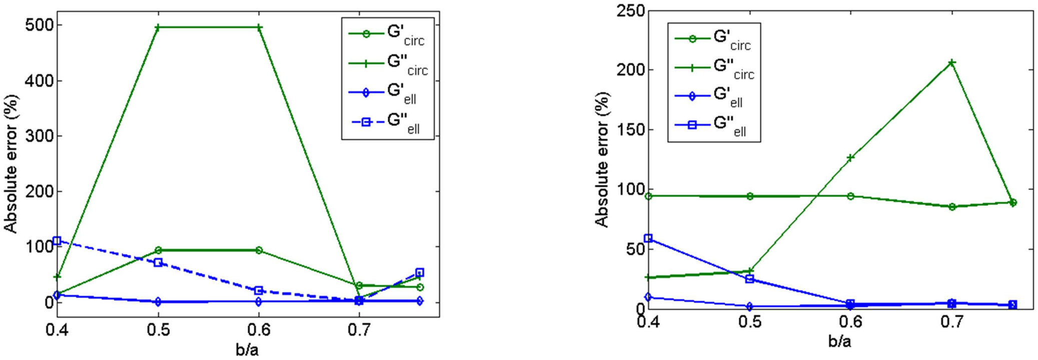

(a) (b)

Figure 13 Errors on inclusion storage and loss moduli obtained by applying an inverse problem, based on a cylindrical shear wave scattering model (Hadj Henni *et al*., 2008) denoted by subscript "circ" and elliptical model ("ell"), to displacement profiles corresponding to various *b/a* ratios. Hard case with *G''*/*G'* = 0.05 (a) and *G''*/*G'* = 0.5 (b) .

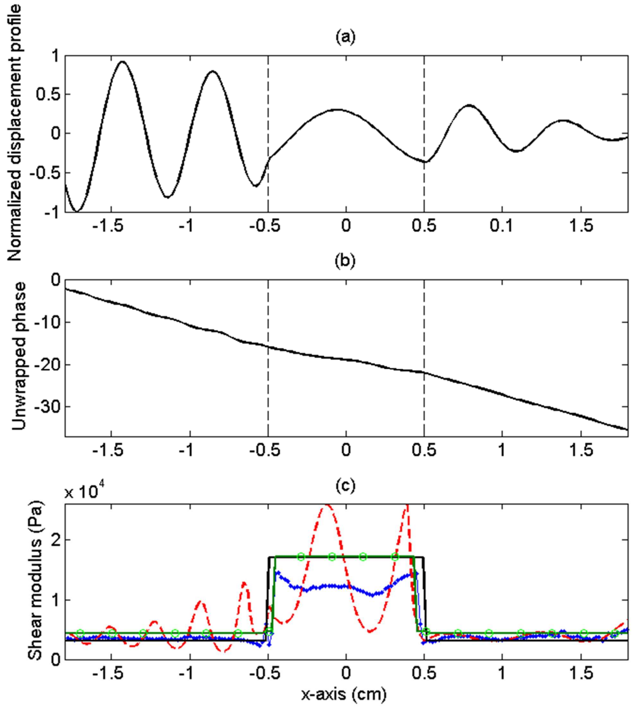

Figure 14. (a) Simulated displacement profile along the large axis of the hard inclusion (configuration B_{th} of table 1). (b) Unwrapped phase corresponding to the displacement profile in (a). (c) Shear moduli obtained using the direct inversion method (dotted blue line), the phase gradient method (dashed red line), the time-of-flight method (green line, circles) and simulated shear moduli (full black line).

Table 1. Mechanical parameters, excitation frequencies and incidence angles used in the forward problem approach; subscript *Th* indicates “theory”.

Medium	G_{incl} *(kPa)*	G_{surr} *(kPa)*	*f* (*Hz*)	Incidence (*deg*)
Soft A_{Th}	$2.4 + i\,0.09$	$17 + i\,1.0$	250	-15
Hard B_{Th}	$17 + i\,0.94$	$3 + i\,0.19$	300	20

Table 2. Agar and gelatin concentrations (in % of water weight) for phantoms *A* and *B* mimicking the theoretical conditions of table 1.

Phantom	Inclusion		Surrounding medium	
	Agar (%)	Gelatin (%)	Agar (%)	Gelatin (%)
Soft A_{Exp}	1	3	3	4
Hard B_{Exp}	3	5	1	3

Table 3. Means and standard deviations of estimated storage and loss moduli for inclusions and surrounding media; subscript *Exp* indicates “experiments”.

Phantom	G_{incl}' *(kPa)*	G_{incl}'' *(kPa)*	G_{surr}' *(kPa)*	G_{surr}'' *(kPa)*
Soft A_{Exp}	2.24 ± 0.09	0.32 ± 0.09	16.40 ± 0.09	2.26 ± 1.34
Hard B_{Exp}	15.67 ± 0.12	2.3 ± 0.19	5.0 ± 0.03	0.32 ± 0.03

REFERENCES

Abramovitz M and Stegun 1965 *Handbook of Mathematical Functions,* I eds: Dover Publications.

Achenbach J D 1973 *Wave propagation in elastic solids,* Amsterdam, Holanda: North-Holland, Elsevier.

American College of Radiology 2007 *ACR Practice guideline for the performance of breast ultrasound examination* 569-73

Andersen E S, Christensen P B and Weis N 2009 Transient elastography for liver fibrosis diagnosis, *European Journal of Internal Medicine* **20** 339-42

Bercoff J, Tanter M and Fink M 2004 Supersonic shear imaging: a new technique for soft tissue elasticity mapping, *IEEE Trans. Ultrason. Ferroelectr. Freq. Control* **51** 396-409

Bercoff J, Chaffai S, Tanter M, Sandrin L, Catheline S, Fink M, Gennisson J L and Meunier M 2003 In vivo breast tumor detection using transient elastography, *Ultrasound in Medicine & Biology* **29** 1387-96

Berg W A, Cosgrove D O, Doré C J, Schäfer F K W, Svensson W E, Hooley R J, Ohlinger R, Mendelson E B, Balu-Maestro C, Locatelli M, Tourasse C, Cavanaugh B C, Juhan V, Stavros A T, Tardivon A, Gay J, Henry J-P, Cohen-Bacrie C for the BEI 2012 Shear-wave elastography improves the specificity of breast US: The BE1 Multinational Study of 939 Masses, *Radiology* **262** 435-49

Bharat S, Techavipoo U, Kiss M Z, Liu W and Varghese T 2005 Monitoring stiffness changes in lesions after radiofrequency ablation at different temperatures and durations of ablation, *Ultrasound in Medicine & Biology* **31** 415-22

Castaneda B, Hoyt K, Westesson K, An L, Baxter L, Joseph J, Strang J, Rubens D and Parker K 2009 Performance of three-dimensional sonoelastography in prostate cancer detection: a comparison between ex vivo and in vivo experiments, *Proc. IEEE Ultrason. Symp.* 519-22

Catheline S, Gennisson J L, Delon G, Fink M, Sinkus R, Abouelkaram S and Culioli J 2004 Measurement of viscoelastic properties of homogeneous soft solid using transient elastography: An inverse problem approach, *The Journal of the Acoustical Society of America* **116** 3734-41

Chaos-Cador L 2002 Mathieu functions revisited: matrix evaluation and generating functions, *Revista Mexicana de Fisica* **48** 67-75

Chen S, Fatemi M and Greenleaf J F 2004 Quantifying elasticity and viscosity from measurement of shear wave speed dispersion, *The Journal of the Acoustical Society of America* **115** 2781-5

Cho N, Jang M, Lyou C Y, Park J S, Choi H Y and Moon W K 2012 Distinguishing benign from malignant masses at breast US: Combined US elastography and color Doppler US — Influence on Radiologist Accuracy, *Radiology* **262** 80-90

Chérin E, Williams R, Needles A, Liu G, White C, Brown A S, Zhou Y-Q and Foster F S 2006 Ultrafast frame rate retrospective ultrasound microimaging and blood flow visualization in mice in vivo, *Ultrasound in Med. & Biol* **32** 683-91

Deffieux T, Gennisson J L, Bercoff J and Tanter M 2011 On the effects of reflected waves in transient shear wave elastography *IEEE Transactions on Ultrasonics, Ferroelectrics and Frequency Control,* **58** 2032-5

Deffieux T, Montaldo G, Tanter M and Fink M 2009 Shear wave spectroscopy for in vivo quantification of human soft tissues visco-elasticity, *IEEE Trans. Med. Imaging* **28** 313-22

Faran J and James J 1951 Sound Scattering by Solid Cylinders and Spheres, *The Journal of the Acoustical Society of America* **23** 405-18

Greif J M 2010 Mammographic screening for breast cancer: An invited review of the benefits and costs, *The Breast* **19** 268-72

Hadj Henni A, Schmitt C and Cloutier G 2008 3D transient and harmonic shear-wave scattering by a soft cylinder for dynamic vascular elastography, *The Journal of the Acoustical Society of America.* **124** 2394-405

Hadj Henni A, Schmitt C and Cloutier G 2010 Shear wave induced resonance elastography of soft heterogeneous media, *J. Biomech.* **43** 1488-93

Hadj Henni A, Schmitt C, Tremblay M E, Hamdine M, Heuzey M C, Carreau P, Cloutier G 2011 Hyper-frequency viscoelastic spectroscopy of biomaterials, *Journal of the Mechanical Behavior of Biomedical Materials* **4**, 1115-22

Hadj Henni A, Schmitt C, Trop I and Cloutier G 2012 Shear wave induced resonance elastography of spherical masses with polarized torsional waves, *Applied Physics Letters* **100,** 133702(1)-133702(5)

Hiltawsky K M, Krüger M, Starke C, Heuser L, Ermert H and Jensen A 2001 Freehand ultrasound elastography of breast lesions: clinical results, *Ultrasound in Medicine & Biology* **27** 1461-9

Jatoi I, Zhu K, Shah M and Lawrence W 2006 Psychological distress in U.S. women who have experienced false-positive mammograms, *Breast Cancer Research and Treatment* **100** 191-200

Keyzer-Dekker C M G, De Vries J, van Esch L, Ernst M F, Nieuwenhuijzen G A P, Roukema J A and van der Steeg A F W 2012 Anxiety after an abnormal screening mammogram is a serious problem, *The Breast* **21** 83-8

Klein J, McLaughlin J, and Renzi D 2012 Improving arrival time identification in transient elastography, *Physics in Medicine and Biology* **57** 2151-68

Leon F, Chati F and Conoir J-M 2004 Modal theory applied to the acoustic scattering by elastic cylinders of arbitrary cross section, *The Journal of the Acoustical Society of America* **116** 686-92

Lerner R, Huang S and Parker K 1990 ‘Sonoelasticity’ images derived from ultrasound signals in mechanically vibrated tissues, *Ultrasound Med. Biol.* **16** 231-9

Madjar H and Mendelson E B eds 2008 *The Practice of Breast Ultrasound: Techniques, Findings, Differential Diagnosis*: Stuttgart,New York:Thieme Publishing Group

Mariappan Y K, Glaser K J and Ehman R L 2010 Magnetic resonance elastography: A review, *Clinical Anatomy* **23** 497-511

McLaughlin J, Renzi D, Yoon J R, Ehman R L and Manduca A 2006 Variance controlled shear stiffness images for MRE data. In: *3rd IEEE International Symposium on Biomedical Imaging: Nano to Macro, 2006,* 960-3

Mitka M 2007 New ultrasound “elasticity” technique may reduce need for breast biopsies, *JAMA: The Journal of the American Medical Association* **297** 455

Montagnon E, Hissoiny S, Després P, Cloutier G 2012, Real-time processing in dynamic ultrasound elastography: A GPU-based implementation using CUDA, *Inter. Conf. on Information Sciences, Signal Processing and their Applications*, 472-477

Muthupillai R, Lomas D J, Rossman P J, Greenleaf J F, Manduca A and Ehman R L 1995 Magnetic-resonance elastography by direct visualization of propagating acoustic strain waves, *Science* **269** 1854-7

Nightingale K, McAleavey S and Trahey G 2003 Shear-wave generation using acoustic radiation force: in vivo and ex vivo results, *Ultrasound in Medicine & Biology* **29** 1715-23

NVIDIA CUDA 2008 *Programming Guide*: http://developer.download.nvidia.com

Ophir J, Cespedes I, Ponnekanti H, Yazdi Y and Li X 1991 Elastography: a quantitative method for imaging the elasticity of biological tissues, *Ultrasonic Imaging* **13** 111-34

Palmeri M L, Wang M H, Dahl J J, Frinkley K D and Nightingale K R 2008 Quantifying hepatic shear modulus in vivo using acoustic radiation force, *Ultrasound in Medicine & Biology* **34** 546-58

Parker K J, Doyley M M, Rubens D J 2011 Imaging the elastic properties of tissue: the 20 year perspective, *Physics in Medicine and Biology* **56** R1-29

Plewes D B, Bishop J, Samani A and Sciaretta J 2000 Visualization and quantification of breast cancer biomechanical properties with magnetic resonance elastography, *Phys. Med. Biol.* **45** 1591-610

Rudenko O V, Sarvazyan A P and Emelianov S Y 1996 Acoustic radiation force and streaming induced by focused nonlinear ultrasound in a dissipative medium, *The Journal of the Acoustical Society of America* **99** 2791-8

Samani A, Zubovits J, Plewes D 2007 Elastic moduli of normal and pathological human breast tissues: an inversion-technique-based investigation of 169 samples, *Physics in Medicine and Biology* **52** 1565-76

Sandrin L, Tanter M, Catheline S and Fink M 2002 Shear modulus imaging with 2-D transient elastography, *IEEE Trans Ultrason Ferroelectr Freq Control* **49** 426-35

Sarvazyan A P, Rudenko O V, Swanson S D, Fowlkes J B and Emelianov S Y 1998 Shear wave elasticity imaging: A new ultrasonic technology of medical diagnostics, *Ultrasound in Medicine and Biology* **24** 1419-35

Schaefer F K W, Heer I, Schaefer P J, Mundhenke C, Osterholz S, Order B M, Hofheinz N, Hedderich J, Heller M, Jonat W and Schreer I 2011 Breast ultrasound elastography—Results of 193 breast lesions in a prospective study with histopathologic correlation, *European Journal of Radiology* **77** 450-6

Schmitt C, Hadj Henni A and Cloutier G 2011 Characterization of blood clot viscoelasticity by dynamic ultrasound elastography and modeling of the rheological behavior, *Journal of Biomechanics* **44** 622-9

Schmitt C, Montagnon E, Hadj Henni A, Qi S, Cloutier G 2013 Shear wave induced resonance elastography of venous thrombi: A proof-of-concept, *IEEE Trans. Med. Imag,* in press

Seltzer M H 1997 Preoperative prediction of open breast biopsy results, *Cancer* **79** 1822-7

Seyyed M H and Sanaei R 2008 Ultrasonic scattering by a fluid cylinder of elliptic cross section, including viscous effects, *IEEE Trans. Ultrason. Ferroelect. Freq. Contr.* **55** 391-404

Sinkus R, Tanter M, Xydeas T, Catheline S, Bercoff J and Fink M 2005 Viscoelastic shear properties of in vivo breast lesions measured by MR elastography, *Magn Reson. Imaging* **23** 159-65

Sridhar M, Liu J and Insana M 2007 Viscoelasticity imaging using ultrasound: parameters and error analysis, *Phys. Med. Biol.* **52** 2425-43

Stamnes J J 1995 Exact two-dimensional scattering by perfectly reflecting elliptical cylinders, strips and slits, *Pure and Applied Optics: Journal of the European Optical Society Part A* **4** 841-55

Sugimoto T, Ueha S and Itoh K 1990 Tissue hardness measurement using the radiation force of focused ultrasound, *Proc. IEEE Ultrason. Symp.* 1377-80

Tanter M, Bercoff J, Athanasiou A, Deffieux T, Gennisson J L, Montaldo G, Muller M, Tardivon A and Fink M 2008 Quantitative assessment of breast lesion viscoelasticity: initial clinical results using supersonic shear imaging, *Ultrasound Med Biol.* **34** 1373-86

Thittai A K, Galaz B and Ophir J 2010 Axial-shear strain distributions in an elliptical inclusion model: Experimental validation and in vivo examples with implications to breast tumor classification, *Ultrasound in Medicine & Biology* **36** 814-20

Valtorta D, Mazza E 2005 Dynamic measurement of soft tissue viscoelastic properties with a torsional resonator device, *Medical Image Analysis* **5**, 481-90

Vappou J, Maleke C, Konofagou E E 2009 Quantitative viscoelastic parameters measured by harmonic motion imaging, *Physics in Medicine and Biology* **54** 3579-94

White R M 1958 Elastic wave scattering at a cylindrical discontinuity in a solid, *The Journal of the Acoustical Society of America* **30** 771-85

Wojcinski S, Farrokh A, Weber S, Thomas A, Fischer T, Slowinski T, Schmidtand W and Degenhardt F 2010 Multicenter study of ultrasound real-time tissue elastography in 779 cases for the assessment of breast lesions: improved diagnostic performance by combining the BI-RADS ® -US classification system with sonoelastography, *Ultraschall Med.* **31** 484-91